



Power Electronic Systems
Laboratory

© 2016 IEEE

Proceedings of the Southern Power Electronics Conference (SPEC 2016), Auckland, New Zealand, December 5-8, 2016

Impact of Iron Dust on Electromechanical Systems: A Case Study

M. Flankl,
A. Tüysüz,
J. W. Kolar

This material is published in order to provide access to research results of the Power Electronic Systems Laboratory / D-ITET / ETH Zurich. Internal or personal use of this material is permitted. However, permission to reprint/republish this material for advertising or promotional purposes or for creating new collective works for resale or redistribution must be obtained from the copyright holder. By choosing to view this document, you agree to all provisions of the copyright laws protecting it.



Eidgenössische Technische Hochschule Zürich
Swiss Federal Institute of Technology Zurich

Impact of Iron Dust on Electromechanical Systems: A Case Study

Michael Flankl, Arda Tüysüz and Johann W. Kolar
Power Electronic Systems Laboratory
Swiss Federal Institute of Technology (ETH Zurich)
Physikstrasse 3
8092 Zurich, Switzerland
Email: {flankl, tuysuz, kolar}@lem.ee.ethz.ch

Abstract— Several actuators (e.g. permanent magnet (PM) machines, magnet valves), sensors (e.g. reed sensors, Hall sensors, inductive proximity switches) and emerging inductive energy harvesting systems rely on a clean environment and/or well-defined magnetic conditions. However, in industrial environments iron dust or iron powder may be present, as e.g. resulting from machining, i.e. drilling or milling of mechanical parts or from mechanical wear, and could accumulate in the vicinity of magnetic components. Accordingly, a model for describing the magnetostatic properties of iron dust is required for analyzing a potentially negative impact on the operating behavior. The model derived in this paper is based on the B-H curve of an underlying base material (C45E steel in the presented case) and two further coefficients, representing the influence of powder density and the imperfect magnetic junction at the interfaces between iron particles. The model is then utilized for investigating the influence of iron dust on the operation of a recently introduced kinetic energy harvesting (KEH) system, as a case study. Three-dimensional finite element method (3-D FEM) simulations show that in this case the flux is actually enhanced by iron dust accumulated in front of the harvester. The paper concludes with an experimental verification of the iron dust B-H model and an experimental analysis of the KEH performance degradation due to iron dust.

I. INTRODUCTION

In industrial environments, iron dust or iron powder may be present, as a by-product of machining (e.g. drilling or milling) of mechanical parts or resulting from mechanical wear. If accumulated in critical locations, iron dust may impair the safe operation of magnetic actuators (e.g. permanent magnet (PM) machines, induction machines, magnet valves) or sensors (e.g. reed sensors, Hall sensors, inductive proximity switches) that rely on a clean environment and/or well-defined magnetic conditions. Moreover, emerging inductive energy harvesting systems, which were recently discussed in various publications [1–9], could be exposed to iron dust in their environments. Since the operating principle of these energy harvesters is based on building up a strong magnetic field, clearly, their performance could be influenced by iron dust collected by this magnetic field.

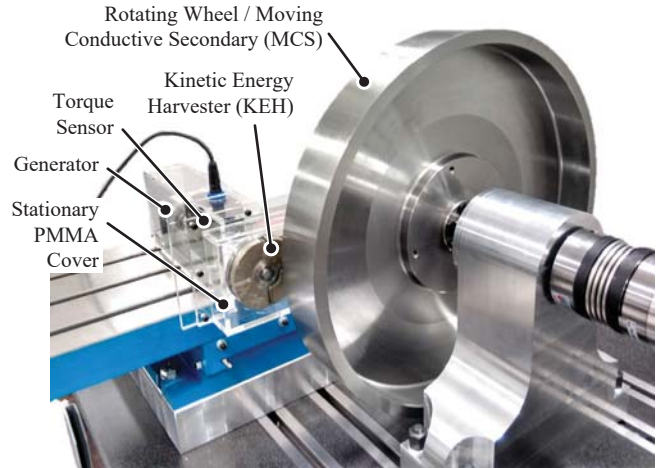


Fig. 1: Kinetic energy harvester (KEH) test setup with torque sensor and generator [1]. The test setup is used in this work to analyze the impact of iron dust on the output power characteristics of a KEH.

Such a system, which is analyzed in this work as a case study, is the kinetic energy harvester (KEH) recently proposed in [1, 2]. It is shown in **Fig. 1** mounted in a test setup, which allows the analysis of various operating conditions and KEH geometries.

The system harvests energy from a moving conductive secondary (MCS) without mechanical contact, as its operation is purely based on eddy-current coupling [1]. This allows to enclose the KEH with a stationary cover, forming a robust, encapsulated system. A mechanical output power of $P_{\text{mech}} \approx 10$ W can be achieved for an air gap of $g_{\text{KEH}} = 10$ mm and a KEH diameter of $2r_1 = 75$ mm, when the speed of a MCS made of steel is $v_2 = 22$ m/s.

However, the presence of iron dust accumulated from the environment could potentially short circuit magnetic field lines from the PMs of the harvester to the MCS and accordingly change its performance. A stationary Polymethyl methacrylate (PMMA) cover is mounted on the setup in **Fig. 1** and the

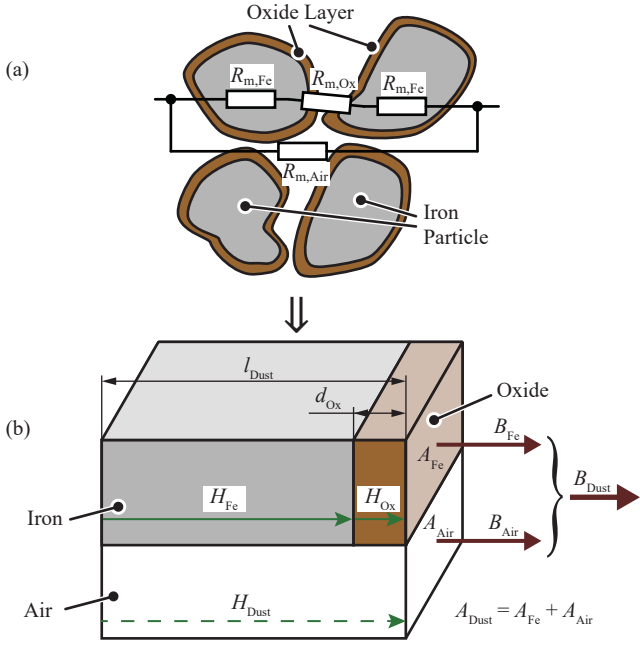


Fig. 2: (a) Grain model of iron dust with oxide layer, indicating the flux paths within a dust particle ($R_{m,Fe}$), at the junction between two particles ($R_{m,Ox}$) and a path, bypassing the dust particles ($R_{m,Air}$). (b) Simplified equivalent model for deriving the B-H curve for iron dust/powder.

impact of an accumulated iron dust layer in front of the cover is investigated in this paper.

In **Sec. II**, a magnetostatic model of iron dust/iron powder is derived and verified with magnetic measurements on an iron dust sample. **Sec. III** estimates the maximum iron dust layer thickness, which would accumulate on the KEH cover considering the force equilibrium on a bulk of dust. **Sec. IV** analyzes the actual KEH air gap flux change under the presence of iron dust with three-dimensional finite element method (3-D FEM) simulations. Finally, measurements of the built up iron dust layer thickness and measurements on the KEH performance degradation due to iron dust in **Sec. V** verify the provided models. **Sec. VI** concludes this work.

II. MAGNETOSTATIC MODELING OF IRON DUST

Firstly, a representative magnetic model for iron dust, whose B-H curve is depicted in **Fig. 3**, shall be derived in order to be employed for evaluating the influence of iron dust on the KEH's operation. The authors would like to state that the model derived in the following might also be applied for iron powder (higher density, non-oxidized grains) under some limitations. **Fig. 2(a)** depicts the assumed properties of the iron dust qualitatively. The magnetic reluctance of the interior of a grain and the oxide layer are indicated with $R_{m,Fe}$ and $R_{m,Ox}$ respectively. A certain low-permeable layer (oxide

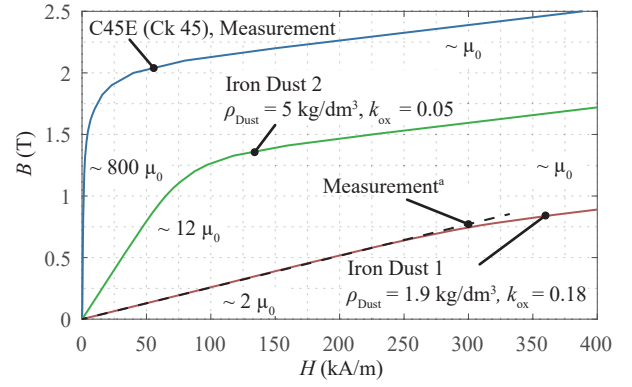


Fig. 3: B-H magnetization curve for carbon steel C45E and the derived iron dust model.

^a Extrapolated B-H curve of an iron dust sample with measured $\mu = 2 \mu_0$.

layer) is assumed on the grains' surfaces, which can be found on probes of iron dust accumulated in industrial environments due to oxidation. Moreover, the introduced reluctance $R_{m,Ox}$ represents also the obviously imperfect magnetic junction at the boundaries between iron particles due to oxide and geometry mismatch in the model formulation. Furthermore, even if the grains of iron dust are densely packed, the filling factor is lower than unity. Similarly, the effective iron cross section is reduced and a flux path in the remaining air is present. This effect is represented with $R_{m,Air}$ in parallel to the main flux path.

In order to describe the magnetic properties of iron dust, which is expected to show significantly different magnetic behavior than solid iron, a simplified B-H characteristic based on the equivalent model depicted in **Fig. 2(b)** can be employed

$$H_{Dust} = H_{Fe}(B_{Fe}) (1 - k_{Ox}) + \frac{B_{Fe}}{\mu_{Ox}} k_{Ox} \quad (1a)$$

$$B_{Dust} = k_{Fe} \cdot B_{Fe} + (1 - k_{Fe}) \cdot \mu_0 H_{Dust} \quad (1b)$$

$$k_{Ox} := \frac{d_{Ox}}{l_{Dust}} \quad (1c)$$

$$\frac{V_{Fe}}{V_{Dust}} = \frac{A_{Fe}}{A_{Dust}} \cdot \frac{l_{Dust} - d_{Ox}}{l_{Dust}} = \frac{\frac{m_{Dust} - m_{Ox}}{\rho_{Fe}}}{\frac{m_{Dust}}{\rho_{Dust}}} \quad (1d)$$

$$k_{Fe} := \frac{A_{Fe}}{A_{Dust}} \approx \frac{\rho_{Dust}}{\rho_{Fe}} \quad (1e)$$

The input parameters of this equation based model are an underlying iron particle B-H curve (technically, its inverse $H_{Fe}(B_{Fe})$) and parameters for the iron dust: density ρ_{Dust} , grain size l_{Dust} , effective oxide layer thickness d_{Ox} and oxide layer permeability μ_{Ox} (cf. **Fig. 2b**). The effective oxide layer thickness d_{Ox} models the imperfect magnetic junction at the interfaces between iron particles due to oxide and geometry

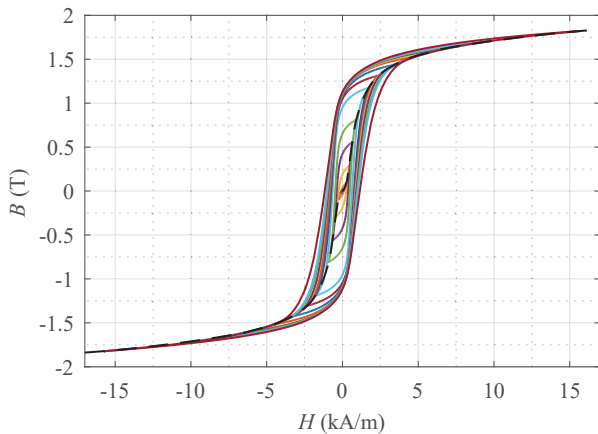


Fig. 4: Measured (on a ring specimen) hysteresis curves of carbon steel C45E (old norm Ck45) at $f = 1$ Hz excitation frequency.

mismatch between the grains, and is therefore larger than a physically measurable oxide thickness on an iron particle's surface.

In order to compute the actual iron dust B-H curve with the implicit formulation in (1), B_{Fe} of the assumed raw material is swept and H_{Dust} , B_{Dust} are obtained.

For this study, carbon steel C45E is selected as the raw material of iron dust as it could result from mechanical wear in an industrial environment. Its B-H curve has been measured electrically with a ring specimen and the hysteresis curves for different amplitudes of magnetic field strength H are depicted in Fig. 4. In Fig. 3, two B-H curves of iron dust with the therein specified parameters are shown.

The parameters k_{Ox} and k_{Fe} for the first sample of iron dust, denoted as iron dust 1 in the following were selected such that they agree with the density measurement $\rho_{Dust} = 1.9 \text{ kg/dm}^3$ and hysteresis measurements of an iron dust sample, depicted in Fig. 5. For measuring the B-H curve of iron dust, a setup as illustrated in Fig. 6 was built. The 3-D printed, hollow core body was filled with an iron dust sample through the filling opening without external compression. Afterwards, the filling opening was closed with a Polyethylene terephthalate (PET) electrical insulation tape with $60 \mu\text{m}$ thickness; a sensing coil with $N_2 = 400$ turns and $d_2 = 0.315 \text{ mm}$ diameter and an excitation coil with rectangular cross section of $0.8 \text{ mm} \times 2 \text{ mm}$ and $N_1 = 226$ were wound around the closed and filled core body. The iron dust sample at hand was obtained by letting commercially available steel powder [10] with specified grain size in the range of $150 \mu\text{m} \leq l_{Dust} \leq 212 \mu\text{m}$ corrode in a moisture environment for 48 hours, as it would occur in the targeted environment of the energy harvesting system at hand.

On the other hand, the parameters for another sample of iron

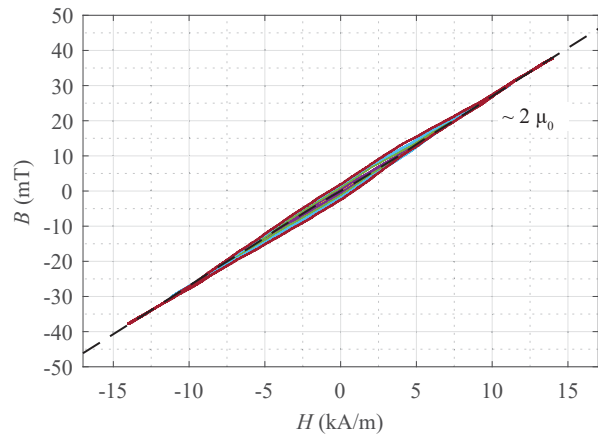


Fig. 5: Measured (on the ring specimen of Fig. 6) hysteresis curves of an iron dust sample at $f = 50$ Hz excitation frequency.

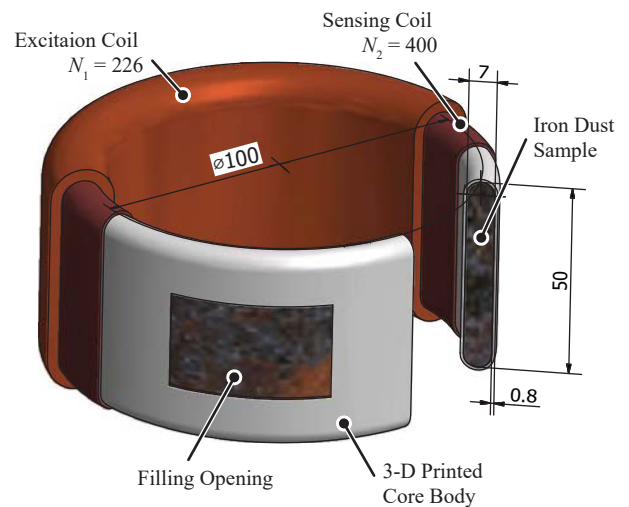


Fig. 6: Setup for measuring the B-H curve of iron dust. The iron dust sample is manually inserted in a 3-D printed, hollow core body through the filling opening without external compression. The filling opening is closed with a PET electrical insulation tape with $60 \mu\text{m}$ thickness; the sensing coil and the excitation coil are wound around the closed and filled core body.

dust, iron dust 2, were selected to illustrate the B-H curve of compressed iron dust or iron powder as it could occur in other applications.

It can be found that the density of iron dust affects its saturation flux density and the assumed oxide thickness affects the permeability before saturation. The parameters of iron dust 1 according to Fig. 3 are used for the following considerations.

III. IRON DUST LAYER THICKNESS

Generally, it is of interest how iron dust influences the operation of magnetic sensors, actuators and in this case energy

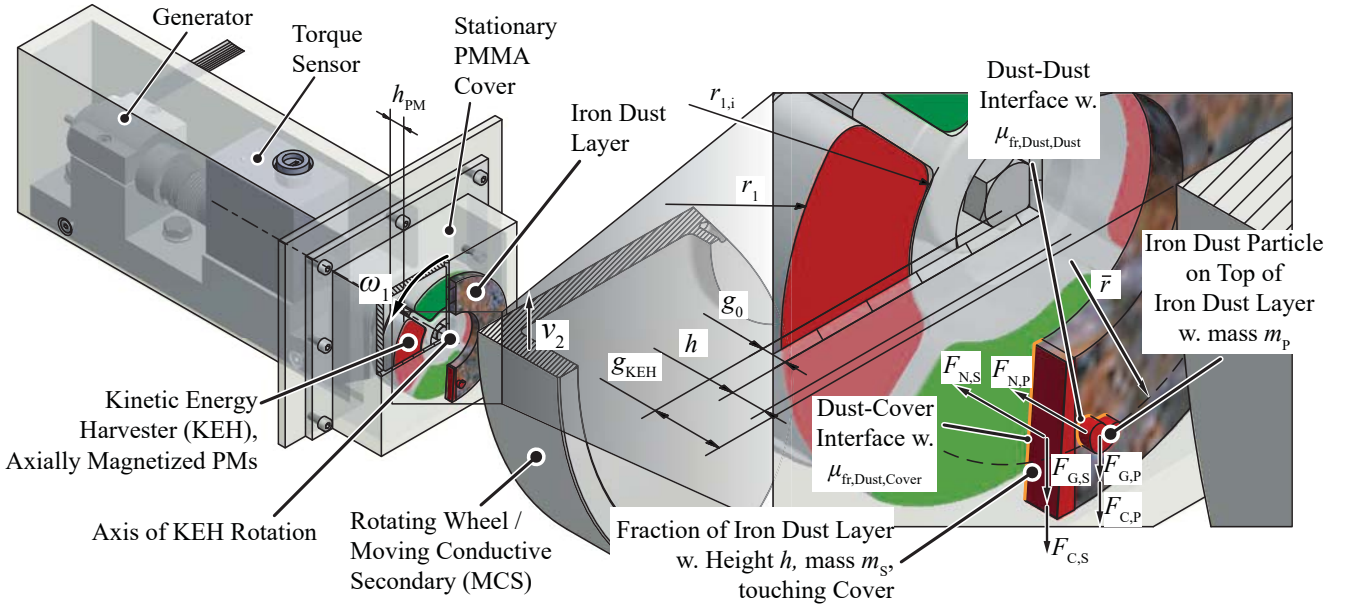


Fig. 7: Illustration of the kinetic energy harvester (KEH) on the test rig. Iron particles in the environment are accumulated in front of the KEH magnets, forming an iron dust layer of thickness h . Two interesting interfaces: dust-dust interface and dust-cover interface are detailed in the zoomed-in view.

harvesters. In a first step, the iron dust thickness h that accumulates in front of the KEH is studied in this section. This information is used later for further 3-D FEM simulations, which will detail the implications of iron dust for the KEH. **Fig. 7** illustrates the test setup with an accumulated iron dust layer of thickness h in front of the KEH PMs.

In an initial experiment, it was observed that dust indeed stays on the KEH cover (cf. **Fig. 7**) and rotates approximately with same speed as the KEH (ω_1), when the system is in operation.

Iron dust gets attached and stays (or rotates with the KEH) as a layer on the KEH cover's surface due to an attracting Maxwell force normal to the PMs and the KEH cover (normal force F_N), which is built up because of the PMs' field and the permeability of iron dust, which is larger than μ_0 . On the other hand, gravitational force (F_G) and centrifugal force (F_C , occurring when the KEH is rotating)

$$F_{G,i} = m_i \cdot g \quad (2a)$$

$$F_{C,i} = m_i \cdot \omega_1^2 \bar{r}, \quad (2b)$$

with \bar{r} being the average distance to the axis of rotation, are acting on the iron dust and are limiting its accumulation.

It has to be noted that it is not the Maxwell force (normal force) that keeps the iron dust in position, but a friction force F_{fr} built up by the normal force and a friction coefficient

$$F_{fr} \leq F_N \mu_{fr}, \quad (3)$$

where the friction coefficient μ_{fr} depends on the material pairing on the interface where it is acting. Therefore, the force equilibria on two interfaces as given in **Fig. 7** are analyzed:

- Dust-cover interface: It is considered that a fraction of iron dust is sliding off the cover due to gravitational and centrifugal force. The apparent friction coefficient is $\mu_{fr,Dust,Cover}$ and all further quantities are denoted with subscript S.
- Dust-dust interface: A dust particle on top of the iron dust layer is observed¹ and it is analyzed if this dust particle is sliding off on the dust layer due to gravitational and centrifugal force. The apparent friction coefficient is $\mu_{fr,Dust,Dust}$ and all further quantities are denoted with subscript P.

Combining the information stated above and norming the expressions by dust fraction mass (m_S) and dust particle mass (m_P),

$$\frac{\overbrace{F_{N,S}(h) \cdot \mu_{fr,Dust,Cover}}^{a_{fr,S}(h)}}{m_S(h)} \geq \overbrace{g + \omega_1^2 \bar{r}}^{a_z(\omega_1)} \quad (4a)$$

$$\text{and } \frac{\overbrace{F_{N,P}(h) \cdot \mu_{fr,Dust,Dust}}^{a_{fr,P}(h)}}{m_P} \geq a_z(\omega_1) \quad (4b)$$

¹This approach could be seen as an analogy to the concept of observing a sample change in electric fields theory.

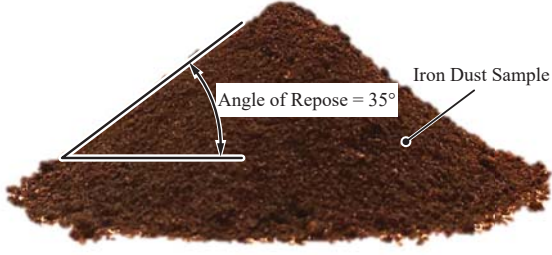


Fig. 8: An angle of repose of 35° was measured experimentally for an iron dust cone of iron dust 1. Accordingly, the grain-to-grain friction coefficient can directly be estimated as $\mu_{fr,Dust,Dust} = \tan 35^\circ$.

must hold, such that an iron dust layer of thickness h stays attached.

Considering a thin built-up iron dust layer, such that $\{a_{fr,S}(h), a_{fr,P}(h)\} < a_z(\omega_1)$ of (4), further iron dust from the environment could be attracted and attached. This could only be restricted by the geometric width of the KEH air gap (cf. g_{KEH} in Fig. 7). On the other hand, assuming for the sake of contradiction that an iron dust particle gets attached to an iron dust layer, such that $a_{fr,S}(h) > a_z(\omega_1)$ or $a_{fr,P}(h) > a_z(\omega_1)$, the iron dust cannot be held by friction and certain particles of iron dust will fall off until the equilibrium is recovered.

A. Estimation of Friction Coefficients

According to (4), a reasonably accurate estimation of friction coefficients $\mu_{fr,Dust,Cover}$ and $\mu_{fr,Dust,Dust}$ is essential for an accurate calculation of dust height thickness.

The grain-to-grain friction coefficient $\mu_{fr,Dust,Dust}$ can be estimated by optically measuring the angle of repose from piled up iron dust (dust cone) as shown in Fig. 8. The angle is formed such that friction can just hold a particle on the pile's surface against the grade resistance and therefore the friction coefficient results as

$$\mu_{fr,Dust,Dust} = \tan 35^\circ = 0.7. \quad (5)$$

An equivalent measurement was conducted for estimating the friction coefficient on the dust-cover interface. For the static case

$$\mu_{fr,Dust,Cover,S} = \tan 20^\circ = 0.38 \quad (6)$$

was measured. However, for the interesting case, where the KEH is rotating with $\omega_1 > 0$ and the iron dust slides on the dust-cover interface, the static friction coefficient does not apply. As the measurement of the friction coefficient on the dust-cover interface under variation of speed difference

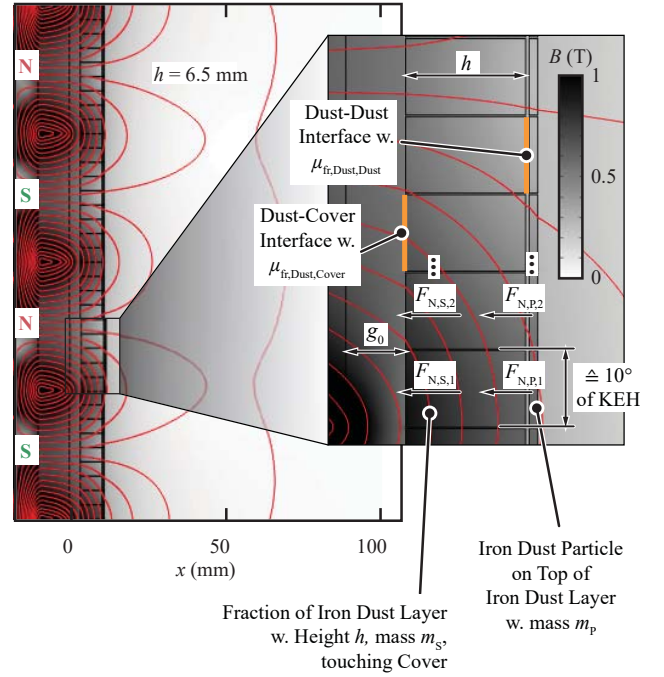


Fig. 9: Problem analyzed with 2-D FEM simulation. The sector magnets are represented as linear bars denoted with N and S in order to study the force equilibria on the dust-cover and dust-dust interfaces.

and under various operating conditions (moisture or oily environment) is out of the scope of this paper, henceforth,

$$\mu_{fr,Dust,Cover} = 0.15 \quad (7)$$

is assumed as a sliding friction coefficient on the dust-cover interface.

TABLE I: Simulation Parameters.

Parameter	Variable	Value
PM inner radius	$r_{1,i}$	17 mm
PM outer radius	r_1	37.5 mm
Avg. dust radius	\bar{r}	27.25 mm
PM height	h_{PM}	10 mm
Gap: PM to MCS	g_{KEH}	10 mm
Gap: PM to cover surf.	g_0	3.5 mm
Number of PMs	n_{PM}	4
PM remanent flux density	B_r	1.4 T
Iron dust density	ρ_{Dust}	1.9 kg/dm ³
Iron dust base material		C45E
Oxide coefficient	k_{Ox}	0.18
Oxide permeability	μ_{Ox}	μ_0
Cover/dust friction coef.	$\mu_{fr,Dust,Cover}$	0.15
Cover/dust friction coef.	$\mu_{fr,Dust,Dust}$	$\tan 35^\circ = 0.7$
KEH rot. speed	ω_1	{0, 50, 100, 200, 400} rad/s

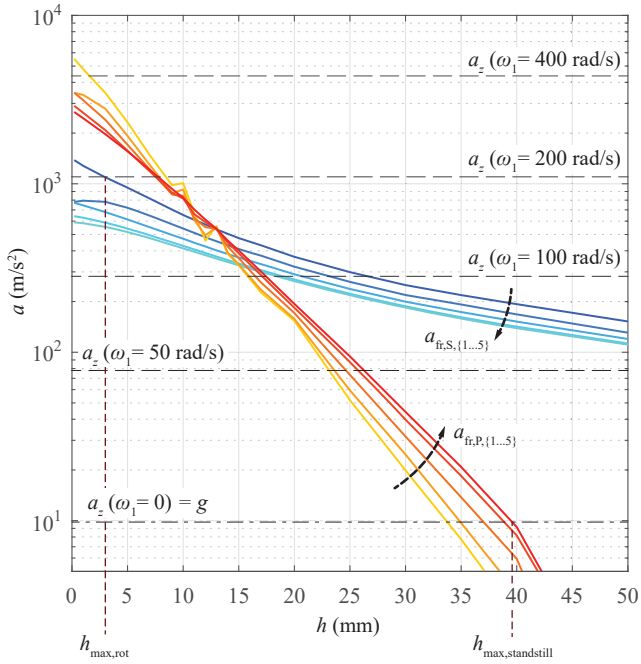


Fig. 10: Retentive accelerations $a_{fr,S,i}(h)$ (on the dust-cover interface) and $a_{fr,P,i}(h)$ (on the dust-dust interface) as result of a 2-D FEM simulation plotted with the pulling acceleration $a_z(\omega_1)$. According to (4), an expected maximum dust layer thickness at standstill ($h_{max,standstill}$) and at rotation ($h_{max,rot}$) can be determined.

B. 2-D FEM Simulations & Results

In order to calculate the attracting force F_N on iron dust, as depicted in **Fig. 9**, a 2-D FEM simulation, where the PMs of the KEH disk are represented as linear bars, is utilized. The stationary 2-D FEM analysis considers the nonlinear magnetic property of iron dust according to the curve specified in **Fig. 3** and further parameters according to **Table I**.

As depicted in **Fig. 7**, the interfaces: dust-dust and dust-cover are analyzed. For the analysis of the dust-cover interface, the iron dust is modeled, as depicted in **Fig. 9**, as blocks of variable dust thickness h (horizontal) and a width (vertical), which is equivalent to 10° of KEH angle (cf. fraction of iron dust layer in **Fig. 9**). The separation in blocks of 10° allows to obtain insight in how the attracting force varies with different positions in front of the KEH magnets. For analyzing the dust-dust interface and hence, computing the force on a dust particle on top of the iron dust layer, small dust particles (modeled as rectangles) are placed on top of the iron dust layer of the 2-D FEM simulation (cf. fraction of iron dust particle in **Fig. 9**).

The attracting forces $F_{N,S,i}$ and $F_{N,P,i}$, acting on the iron dust fractions and the particles respectively, are calculated numerically by the FEM simulation software by the integration

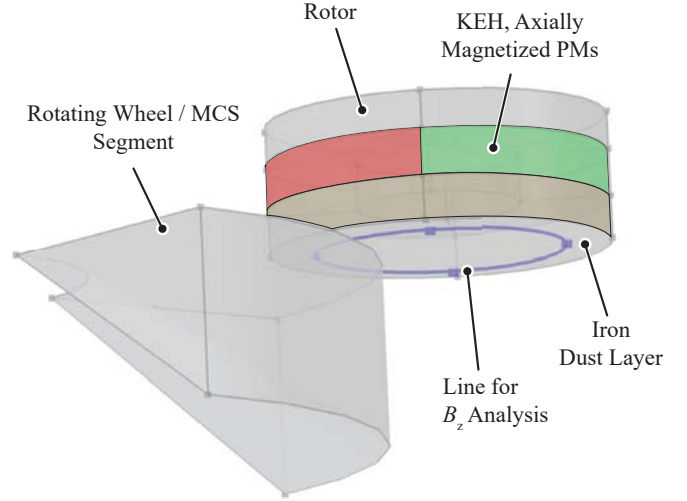


Fig. 11: Illustration of the 3-D simulation model.

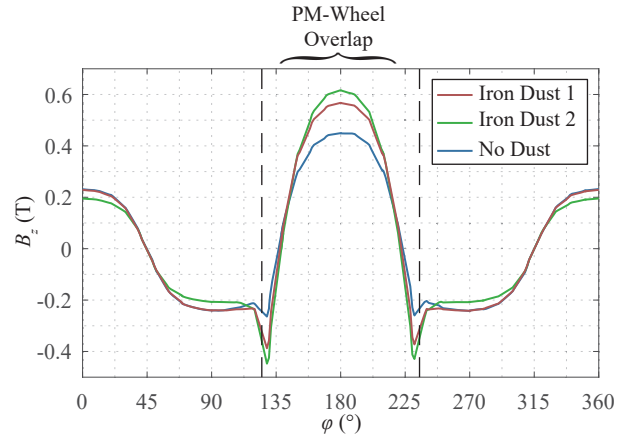


Fig. 12: Flux density in axial direction B_z on the circle shown in **Fig. 11** for the position of one PM fully facing the MCS, showing the increase in flux density due to an iron dust layer in the air gap.

of the Maxwell stress tensor on the fraction's/particle's surface. For obtaining accurate results with this method, a small gap of 0.2 mm is introduced between the fractions/particles in the 2-D FEM simulation. The attracting forces are extracted from the FEM simulation and the retentive accelerations $a_{fr,S,i}(h)$ and $a_{fr,P,i}(h)$ according to (4) are calculated. Results are plotted together with the pulling acceleration $a_z(\omega_1)$ for a set of KEH operating speeds $\omega_1 \in \{0, 50, 100, 200, 400\}$ rad/s in **Fig. 10**. $a_z(\omega_1 = 200$ rad/s) is of particular interest as it is approximately at the KEH rotating speed at maximum power point (MPP) operation with a MCS surface speed of $v_1 = 22$ m/s and the freewheeling speed of the KEH with a MCS surface speed of $v_1 = 11$ m/s.

As both of the equilibrium conditions in (4) must hold, from

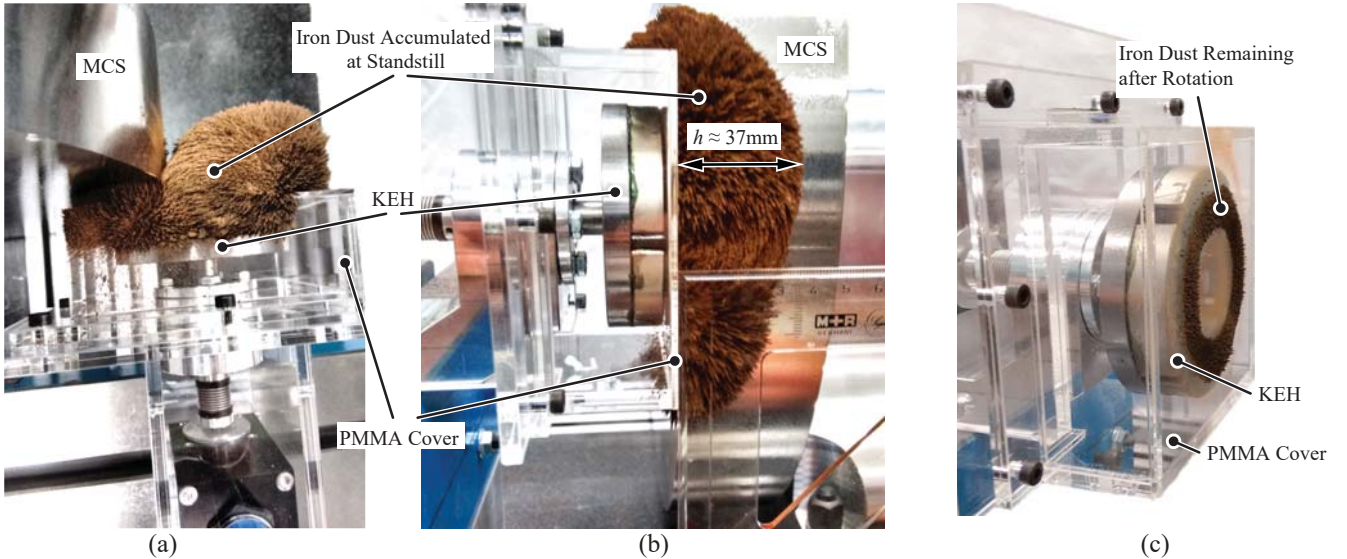


Fig. 13: (a), (b) Photograph of the KEH with manually applied iron dust at standstill. (c) KEH after rotation, showing the remaining iron dust after rotation with $\omega_1 = 200 \text{ rad/s}$.

the results, depicted in **Fig. 10**, can be concluded that

- the force equilibrium on a dust particle at the dust-dust interface is determining the dust layer thickness in standstill, while
- the force equilibrium on a dust fraction at the dust-cover interface is determining the dust layer thickness at rotating speeds $\omega_1 > 100 \text{ rad/s}$.

From **Fig. 10** it can be seen that the expected maximum dust layer thickness on the KEH in standstill is $h_{\text{max,standstill}} \approx 40 \text{ mm}$, whereas the expected maximum dust layer thickness at the interesting rotational speed of $\omega_1 = 200 \text{ rad/s}$ is $h_{\text{max,rot}} \approx 3 \text{ mm}$.

In summary, this section shows that the geometric air gap constraint $g_{\text{KEH}} = 10 \text{ mm}$ limits the dust layer thickness in standstill to $h \leq g_{\text{KEH}} - g_0 = 6.5 \text{ mm}$ in the area, where KEH and MCS overlap. On the other hand, the analysis of friction force between dust layer and the cover during KEH rotation predicts that negligible dust layer ($< 3 \text{ mm}$) remains on the KEH's cover, once the system is running. Measurement results that verify these findings are presented in **Sec. V**.

IV. IMPACT ON KEH FLUX

In this section, it is analyzed how the flux between KEH and MCS is influenced by iron dust in the standstill case, assuming that the air gap is fully filled. The actual geometry (as shown in **Fig. 7**) is simplified in the utilized 3-D FEM simulation setup (cf. **Fig. 11**), which allows to reduce numerical simulation errors and computational time. Simulation parameters according

to **Table I** are employed for the simulation and the axial flux density on the circle indicated in **Fig. 11** is calculated.

The stationary 3-D FEM simulation reveals that at standstill, the flux density in the air gap is increased by the presence of iron dust, for a wide variety of iron dust parameters (ρ_{Dust} and k_{Ox}). This is due to the fact that the iron dust has a permeability significantly lower than iron, but higher than air, which leads to a reduced, but not vanishing, air gap reluctance. **Fig. 12** indicates that the iron dust applied for later experimental results (iron dust 1) increases the peak flux density by $\approx 25\%$.

V. EXPERIMENTAL RESULTS

Finally, measurements with the setup of **Fig. 1** are conducted. Firstly, the predictions of **Sec. III** concerning the built up dust layer thickness in standstill and at rotation of the KEH shall be verified. Iron dust is manually applied to the KEH in standstill until the thickness of the iron dust layer cannot be increased and the force equilibrium on said interfaces is established. **Fig. 13(a)** and **Fig. 13(b)** provide photographs of the KEH setup with iron dust applied during standstill. As predicted in **Sec. III-B**, the air gap between KEH cover and MCS is completely filled with iron dust. Moreover, the calculated maximum built up dust height in standstill $h_{\text{max,standstill}} \approx 40 \text{ mm}$ agrees well with the experimental result of **Fig. 13(b)** of 37 mm .

Moreover, as predicted, the majority of iron dust falls off the harvester once the MCS and the KEH are rotating ($\omega_1 = 200 \text{ rad/s}$). **Fig. 13(c)** shows the remaining iron dust

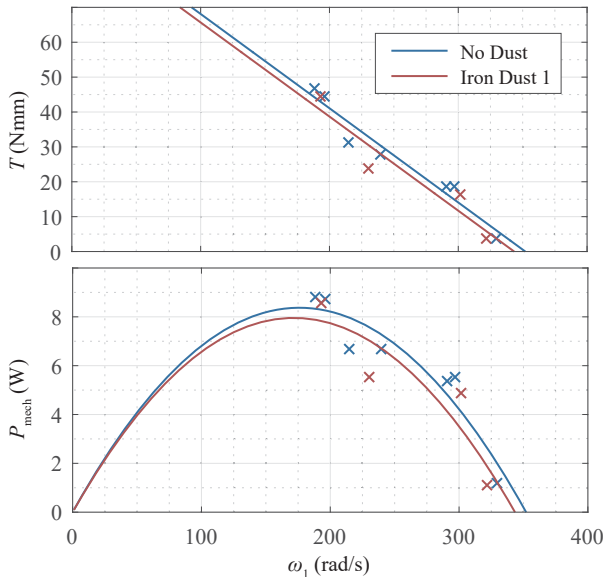


Fig. 14: Measured influence of iron dust on harvested power with constant KEH surface speed $v_2 = 18.8 \text{ m/s}$ and air gap $g_{KEH} = 10 \text{ mm}$. The mechanically harvested torque T and mechanically harvested power P_{mech} is measured with a precision torque sensor as depicted in Fig. 1.

layer after rotating the KEH with $\omega_1 = 200 \text{ rad/s}$, which is in fair agreement with the prediction of Sec. III-B of $h_{max,rot} \approx 3 \text{ mm}$.

Finally, energy harvesting measurements were conducted to conclude the investigation of iron dust impact for the KEH. The measurement result in Fig. 14 show an only insignificant ($\approx -5\%$) degradation of harvested power due to iron dust.

VI. CONCLUSION

In this paper, the B-H characteristic and/or the magnetostatic behavior of iron dust is modeled. The input parameters are the B-H curve of an underlying base material (C45E steel in the presented case) and three further coefficients: k_{Fe} , k_{Ox} and μ_{Ox} . Hysteresis measurements of the base material (C45E) and an iron dust sample are confirming the model. In the case at hand, the iron dust model is utilized to estimate the influence on the operation of magnetic devices at the example of a kinetic energy harvester (KEH). The predicted iron dust layer thickness was confirmed in the experiment and finally, an only insignificant ($\approx -5\%$) degradation of harvested power due to iron dust was measured.

The modeling approach is of general value and it can be used for estimating the thickness of an accumulated iron dust layer thickness and its implication on flux for various magnetic components such as inductive sensors (e.g. inductive proximity switches, PMs of reed sensors) and actuators (e.g.

on the housing of permanent magnet (PM) machines or magnet valves).

In the course of further research a detailed experimental characterization of a variety of iron dust samples (higher density ρ_{Dust} , variable grain size) at a higher magnetic field strength ($H > 200 \text{ kA/m}$) could be performed using a setup in analogy to [11]. This would allow to verify the postulated model entirely or allow to refine the magnetostatic model of iron dust.

VII. ACKNOWLEDGMENT

The authors would like to express their sincere appreciation to Nabtesco Corp., Japan, for the financial and technical support of research on energy harvesting technologies at the Power Electronic Systems Laboratory, ETH Zurich, which provided the basis for achieving the results presented in this paper. In particular, inspiring technical discussions with K. Nakamura, Y. Tsukada and Y. Ono should be acknowledged.

REFERENCES

- [1] M. Flankl, A. Tüysüz, I. Subotic, and J. W. Kolar, "Novel Contactless Axial-Flux Permanent-Magnet Electromechanical Energy Harvester," *Proceedings of the IEEE Applied Power Electronics Conference and Exposition (APEC)*, pp. 623–630, March 2016.
- [2] M. Flankl, A. Tüysüz, and J. W. Kolar, "Outrunner Generator with Optimized Cogging Torque Pattern for an Electromechanical Energy Harvester," *Accepted for publication at the Annual Conference of the IEEE Industrial Electronics Society (IECON)*, October 2016.
- [3] —, "Analysis and Power Scaling of a Single-Sided Linear Induction Machine for Energy Harvesting," *Proceedings of the Annual Conference of the IEEE Industrial Electronics Society (IECON)*, pp. 835–842, November 2015.
- [4] —, "Analysis of a Watt-Range Contactless Electromechanical Energy Harvester Facing a Moving Conductive Surface," *Proceedings of the IEEE Energy Conversion Congress and Exposition (ECCE USA)*, pp. 414–420, September 2015.
- [5] D. Strothmann, "Device For Contactless Current Generation, In Particular Bicycle Dynamo, Vehicle Lighting System And Bicycle," DE Patent WO 2013/004 320 A1, 01 10, 2013.
- [6] Shun-Fu Technology Corp., "Induktionsgenerator," Gebrauchsmuster DE 202 014 100 380 U1, 04 24, 2014.
- [7] Y. H. Kwon and Y. S. Kim, "Analysis of Induced Voltage for Ferrohydrodynamic Energy Harvester using Sloshing Motion," *Proceedings of the International Conference on Electrical Machines and Systems (ICEMS)*, pp. 1671–1675, October 2015.
- [8] B. Lafarge, O. Curea, A. Hacala, and H. Camblong, "Analysis, Design and Simulation of an Electromechanical Energy Harvesting System using a Linear Movement," *First International Conference on Green Energy (ICGE)*, pp. 233–239, March 2014.
- [9] T. v. Bueren and G. Troester, "Design and Optimization of a Linear Vibration-Driven Electromagnetic Micro-Power Generator," *Sensors and Actuators A*, vol. 135, no. 2, pp. 765–775, 2007.
- [10] Iron Powder Corporation of North America. Datasheet Steel Powder S100. checked: September 2016. [Online]. Available: <http://www.iron-powder.com>
- [11] C. Cecile, C. Espanet, Y. Civet, S. Biwersi, and Y. Perriard, "Design and Modelling of a Test Bench to Characterise Magnetic Fluids," *Proceedings of the IEEE International Conference on Advanced Intelligent Mechatronics (AIM)*, pp. 1603–1607, July 2015.